

ENHANCED AND EFFICIENT ISAR IMAGE FOCUSING USING THE DISCRETE GABOR REPRESENTATION IN AN OVERSAMPLING SCHEME

Ji-Hoon Park* and Noh-Hoon Myung

Department of Electrical Engineering, Korea Advanced Institute of Science and Technology (KAIST), 335 Gwahangno, Yuseong-gu, Daejeon 305-701, Korea

Abstract—Inverse synthetic aperture radar (ISAR) imaging is one of the most well-known techniques of radar target recognition. One of the most important issues in ISAR imaging is the improvement of the image smeared by a moving target. In this paper, we propose the discrete Gabor representation (DGR) in an oversampling scheme as an effective means of obtaining a well-focused ISAR image with a short calculation time. In contrast to other linear time-frequency transforms (TFTs), the DGR obtains Gabor coefficients using the analysis window frames derived from the clearly defined Gaussian-type synthesis window. The oversampling scheme of the DGR leads to accurate calculations of the Gabor coefficients, which denote signal time-frequency amplitude. Since each Gabor coefficient is compartmentally assigned to the associated unit cell of the time-frequency grid, the DGR can show an excellent time-frequency concentration and can effectively discriminate the Doppler components of prominent point-scatterers. The application results demonstrate that the DGR not only has enhanced focusing performance but also retains computational efficiency. The DGR in the oversampling scheme is expected to facilitate high-quality ISAR imaging in radar target recognition.

1. INTRODUCTION

A real-world target with complicated motion imparts a time-varying Doppler frequency shift to the radar target signature. Different from the synthetic aperture radar (SAR) images [1–3], the ISAR (inverse SAR) images [4–9] can have severe image smearing problems caused

Received 20 February 2013, Accepted 15 March 2013, Scheduled 20 March 2013

* Corresponding author: Ji-Hoon Park (dydynoel@kaist.ac.kr).

by the time-varying Doppler frequency. This is because conventional ISAR imaging with the Fourier transform (FT) cannot show how frequency components vary with time. For better performance of ISAR imaging in radar target recognition, the smeared ISAR image needs to be focused by compensating for the target motion, which is also called as the ISAR motion compensation [10–14]. Recently, time-frequency transforms (TFTs) have been widely employed in order to effectively reflect the time-dependent characteristic of the Doppler frequency [15–23]. In general, there are two requirements in TFT-based ISAR image focusing. First, the selected TFT should have high time-frequency resolution, which is directly related to accurate representation of the time-dependent Doppler frequency. Second, it is imperative that the ISAR imaging procedure be computationally efficient. That is to say, the TFT operation should be fast enough to be applied in the real-time target recognition process.

Since Chen et al. first introduced the concept of TFT-based radar imaging [15, 16], various time-frequency transforms have been developed for ISAR applications. Linear TFTs, such as the short-time Fourier transform (STFT) and the wavelet transform (WT) are well-known methods and are conceptually simple to implement [8–10]. Despite their operational simplicity, the resolution limitation always arises from the window-induced Heisenberg-Gabor limit. For more enhanced focusing performance, bilinear TFTs [16, 19, 20] and adaptive TFTs with optimization methods [21–23] were subsequently proposed. Although they significantly improved the image smearing problem, these methods were still restrictive in real-time signal processing because of their computational burden. Thus, recently developed methods [24, 25] have concentrated on achieving both accuracy and efficiency in ISAR image focusing.

In this paper, we propose the discrete Gabor representation (DGR) [26–28] as an effective approach for obtaining well-focused ISAR images. In contrast to other linear TFTs, the DGR analytically obtains the analysis window from the given synthesis window. With the oversampling scheme of the DGR [26, 27], Gabor coefficients, derived from the analysis window frames can contain accurate information on the signal time-frequency components. In addition, the DGR compartmentally allocates the Gabor coefficients to the respective unit cells of the time-frequency grid. This property gives the DGR an excellent time-frequency concentration. The DGR also retains computational efficiency and can be easily implemented by slightly modifying the existing STFT. This paper is organized as follows: In Section 2, we briefly introduce the radar signal model and the TFT-based ISAR imaging. The DGR in the oversampling scheme and

its application to ISAR image focusing are discussed in Section 3. Section 4 presents application examples to validate the effectiveness of the DGR in terms of focusing performance and computational efficiency. Finally, conclusions are drawn in Section 5.

2. THE RADAR SIGNAL MODEL AND THE PRINCIPLE OF TFT-BASED ISAR IMAGING

According to the geometrical theory of diffraction (GTD), the scattered field of a complex target at high frequencies can be regarded as being from a set of individual point-scatterers [15]. Based on the GTD model, the radar signal received from the target with K point-scatterers can be represented as

$$s_R(t) = \sum_{k=1}^K A_k \exp \left[-j \frac{4\pi}{\lambda} R(t) \right] \exp \left[-j \frac{4\pi}{\lambda} (x_k \cos \theta(t) - y_k \sin \theta(t)) \right] \quad (1)$$

where λ is the radar wavelength, and (x_k, y_k) and A_k are the position and the scattering amplitude of the k th point scatterer, respectively. The distance $R(t)$ is expressed with the translational motion parameters of the target. With range tracking [15], the first exponential term in Equation (1) is removed. The time-varying rotation angle $\theta(t)$ is assumed to be Ωt where Ω is the angular speed. The rotation-induced Doppler shift derived from Equation (1) is characterized by the time-varying term $\Omega^2 t$ [15, 16]. Thus, for a relatively long coherent processing time (CPT) and a fast angular speed, the FT is replaced by the TFT in ISAR imaging. When the radar transmits a wide-band waveform, such as the stepped-frequency (SF) waveform, the received data is constructed into a 2D format. Using the TFT, the 2D data set is then extended into a 3D ISAR cube, which consists of time samples, (Doppler) frequency samples and range cells (range bins). From the ISAR cube, a 2D range-Doppler image is taken at a particular instant of time samples. This temporal frame shows the focused ISAR image because the time-varying Doppler appears to be approximately constant at each instant. Therefore, for improved ISAR image focusing, we need to select the TFT with high time-frequency resolution. Furthermore, it is desirable that the TFT is computationally efficient since additional data extension is involved in the imaging process described above. Overall procedures of the TFT-based ISAR imaging are illustrated in Figure 1.

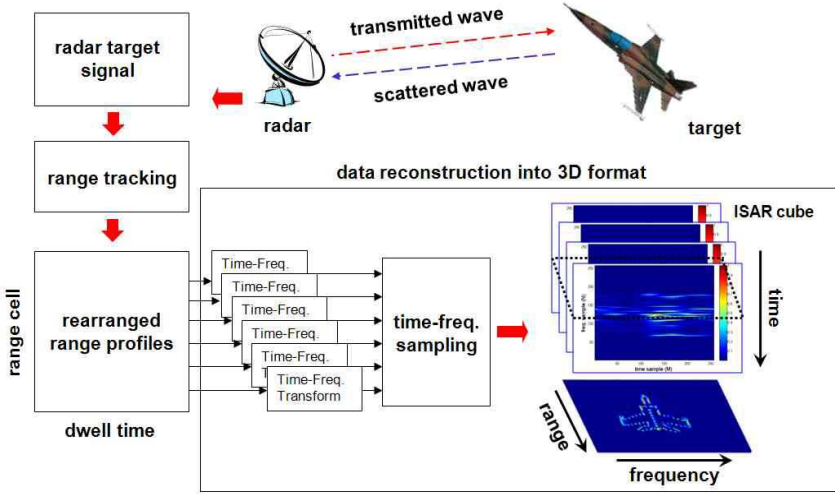


Figure 1. Overall procedures of the TFT-based ISAR imaging.

3. DISCRETE GABOR REPRESENTATION IN AN OVERSAMPLING SCHEME FOR ISAR APPLICATION

3.1. Discrete Gabor Representation of a Signal in the Oversampling Scheme

The Gabor representation and its numerical implementation have been extensively investigated [26–30] since Gabor suggested the signal expression with a discrete set of Gaussian functions. For a discrete-time signal $x[k]$ with a length of N_b , the discrete form of the Gabor representation, namely the DGR, rearranges the signal into the 2D time-frequency grid with M time samples and N frequency samples as shown in Figure 2. The DGR of the signal $x[k]$ consists of the discrete Gabor expansion and the discrete Gabor transform as follows [26]:

$$x[k] = \sum_{m=0}^{M-1} \sum_{n=0}^{N-1} a_{m,n} h_{m,n}[k] = \sum_{m=0}^{M-1} \sum_{n=0}^{N-1} a_{m,n} h[k - m\Delta M] e^{j\frac{2\pi(n\Delta N)k}{N_b}} \quad (2)$$

$$a_{m,n} = \sum_{k=0}^{N_b-1} x[k] \gamma *_{m,n}[k] = \sum_{k=0}^{N_b-1} x[k] \gamma[k - m\Delta M] e^{-j\frac{2\pi(n\Delta N)k}{N_b}} \quad (3)$$

In Equation (2), a_{mn} and $h_{mn}[k]$ are Gabor coefficients and Gabor logons, respectively. The Gabor logons are shifted and modulated versions of the given synthesis window $h[k]$ for the time and frequency

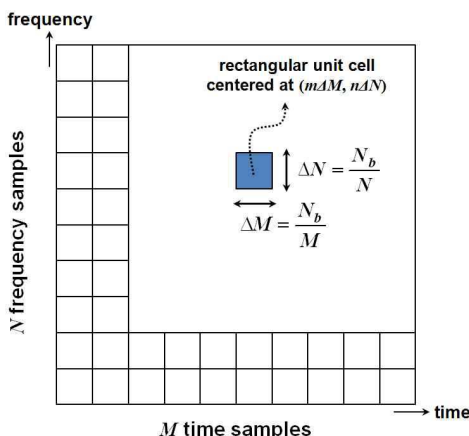


Figure 2. DGR time-frequency grid with a size of $(N \times M)$ and sampling intervals with respect to N_b .

sampling intervals ΔM and ΔN marked in Figure 2. The Gabor expansion tells that the original signal $x[k]$ can be reconstructed by the weighted sum of Gabor logons. From Equation (3), the Gabor coefficients can be obtained from the analysis window frames $\gamma_{m,n}[k]$, shifted and modulated versions of the analysis window $\gamma[k]$. $\gamma[k]$ satisfies the bi-orthogonal condition (Wexler-Raz identity) in conjunction with $h[k]$ such that

$$\sum_{k=0}^{N_b-1} h[k+m\Delta M]\gamma^*[k]e^{-j\frac{2\pi(n\Delta N)k}{N_b}} = \sum_{k=0}^{N_b-1} h_{-m,-n}[k]\gamma^*[k] = \frac{N_b}{NM}\delta_m\delta_n \quad (4)$$

where δ_m denotes the Kronecker delta. According to the Balian-Low theorem [28], however, the time-frequency grid with a size of $(N \times M)$ should be oversampled with respect to the signal length such that

$$N_b = NM/Q \quad (5)$$

where Q is a positive integer and indicates the oversampling ratio. A larger Q means that the signal $x[k]$ is rearranged into a more detailed time-frequency grid. Thus, the DGR in the oversampling scheme leads to interpretational clarity. In addition, the oversampling is equivalent to making the form of $\gamma[k]$ identical to that of $h[k]$. Hence $\gamma[k]$ refined by the oversampling scheme can achieve both the accurate calculation of $a_{m,n}$ and numerical stability [26–28]. Note that Q should be selected in consideration of a compromise between accuracy and efficiency since Q is also related to the computation time. For analytic

determination of $\gamma[k]$ satisfying Equation (4), the Zak transform pair-based method [27] can be considered as follows:

$$\tilde{\gamma}[k, l] = \frac{\tilde{h}[k, l]}{\sum_{i=0}^{Q-1} \left| \tilde{h} \left[k - \frac{i}{Q}, l \right] \right|^2} \quad (6)$$

Here, the tilde denotes the discrete Zak transform defined as the Fourier transform of the signal sequence $x[k + m\Delta M]$ with the basis of $e^{j(m\Delta M)l}$. The analysis window is then obtained by taking the inverse Zak transform of $\tilde{\gamma}[k, l]$. A noticeable characteristic of the DGR is that it analytically calculates $\gamma[k]$ in contrast to other window-based linear TFTs in which the analysis window is provided without taking into account signal reconstruction.

3.2. Discussion on the DGR Application to the ISAR Image Focusing

In this section, we discuss the application of the oversampled DGR to ISAR image focusing using the acquired 2D radar signal. Assuming that the radar signal with the SF waveform is composed of M_p narrow frequency band pulses and N_b sequential groups of pulses (bursts), each time-domain signal extracted along the bursts is rearranged into the $(N \times M)$ time-frequency grid via the DGR as illustrated in Figure 3. Note that the signal length N_b described in the previous section is the same as the number of bursts. The performance of concentrating the signal components on the time-frequency grid is important in TFT-based ISAR imaging. Thus, a Gaussian-type synthesis window is selected in this paper since Gaussian functions can reach the lower bound of the Heisenberg-Gabor limit [28]. The selected $h[k]$ is extended to the Gabor logons, which correspond to respective unit cells of the time-frequency grid centered at $(m\Delta M, n\Delta N)$. Then, $h[k]$ calculates the analysis window $\gamma[k]$ with Equation (6). As explained in the previous section, the DGR in the oversampling scheme yields the refined Gaussian-type analysis window as a decayed form of the originally given synthesis window [29]. With the analysis window frames $\gamma_{m,n}[k]$ the Gabor coefficients $a_{m,n}$ are acquired by Equation (3). According to Equation (2), each Gabor coefficient is determined as the weight of each Gabor logon and represents the time-frequency amplitude of each unit cell with a size of $(\Delta M \times \Delta N)$. Consequently, the linear combination of $a_{m,n}$ and $h_{m,n}[k]$ can reconstruct the original time-domain signal $x[k]$. This is the key difference from the STFT whose expression is given only by (3). Since the STFT uses the arbitrarily given analysis window, it may lead to

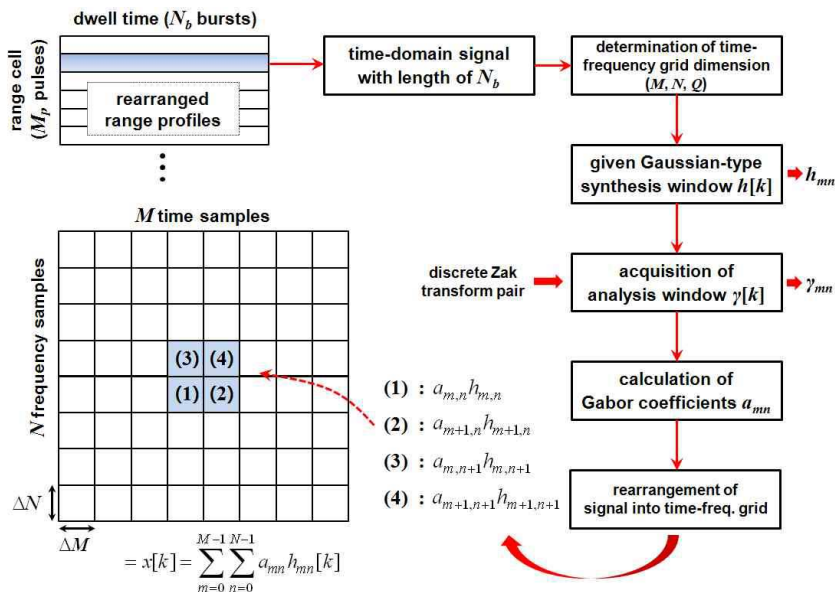


Figure 3. Diagram for application of the oversampled DGR to the rearranged 2D radar received signal.

a lack of completeness of the signal reconstruction and the coefficient (spectrogram) calculation.

From Figure 4 showing the conceptual DGR time-frequency representation, it is seen that the DGR in the oversampling scheme is suitable for the TFT-based ISAR image focusing. The Gabor coefficients (‘amplitude’ in Figure 4) are obtained from the analysis window frames and these frames are related to the Gabor logons, which comprise the time-frequency grid. That is, the Gabor coefficients are compartmentally assigned to the respective unit cells by considering the reconstruction of the original time-domain signal. Furthermore, the oversampling scheme makes each Gabor coefficient denote accurate amplitude in the associated unit cell. Therefore, the DGR in the oversampling scheme is expected to exhibit an excellent concentration of the signal components on the time-frequency grid. In ISAR applications, this characteristic leads to effective discrimination of the Doppler components of prominent point-scatterers. Simultaneously, the DGR appears to suppress other frequency components by compartmental allocation of $a_{m,n}$ and $h_{m,n}[k]$. Apart from the focusing performance, the DGR also retains computational efficiency since it is not an adaptive algorithm that involves searching procedures but

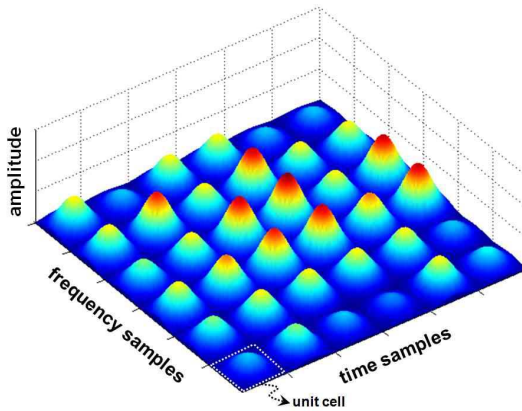


Figure 4. Conceptual DGR time-frequency representation.

can be implemented by simply adding the Zak-transform pair-based determination of $\gamma[k]$ to the existing STFT.

4. DGR APPLICATION TO ISAR IMAGE FOCUSING

4.1. Application to Radar Signals from Ideal Point-scatterer Sets

First, we examine artificial radar signal data from two sets of the ideal point-scatterers using Equation (1). Although the model of ideal point-scatterers does not imitate the actual scattering from a target, it can be a sufficiently good standard for evaluating ISAR imaging performance [15, 18, 31] in a high frequency band. Figure 5 shows actual locations of respective sets of ideal point-scatterers. Table 1 summarizes the parameters related to the simulation. By the rotation speed beyond normal rates and the relatively long CPT, the ISAR images from the FT are severely smeared by the time-varying Doppler frequencies as shown in Figure 6. In this simulation, it was assumed that the translational motion was completely compensated for by the range tracking.

In order to focus the smeared ISAR image, we apply the DGR with an oversampling ratio Q of 32. From Equation (5), the numbers of the time samples and frequency samples (M and N) were selected as 64 and 128, respectively. Thus, each time-domain signal along the 256 bursts is rearranged into a (128×64) time-frequency grid. Note that the number of time samples, which is also the number of temporal frames, is not necessary to be the same as the number of bursts because there is little

Table 1. Parameters related to the simulation with ideal point-scatterer sets.

number of point-scatterers	set 1: 18, set 2: 37
center frequency, bandwidth (BW)	7.75 GHz, 512 MHz
radar signal waveform	stepped-frequency (SF)
number of pulses (M_p)	64
number of bursts (N_b)	256
pulse repetition frequency (PRF)	15 kHz
angular velocity (Ω)	0.5 rad/s

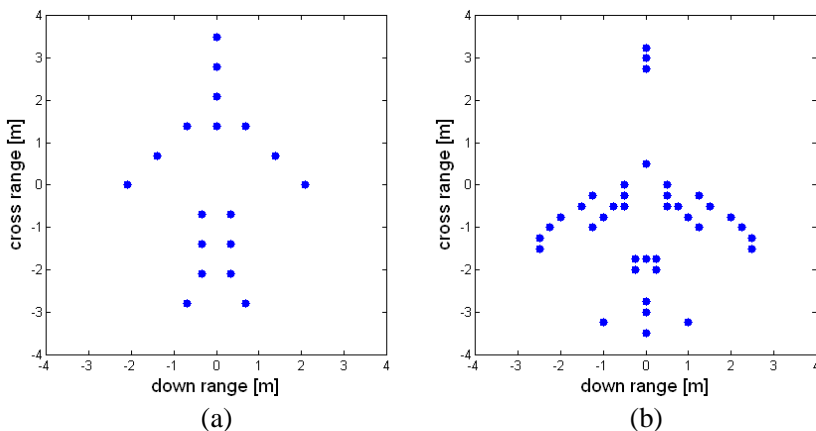


Figure 5. Actual locations of the examined sets of ideal point-scatterers: (a) set 1 and (b) set 2.

Doppler variation between sufficiently dense time samples [15, 16]. In Figure 7, the ISAR images of the point-scatterer set 1 are depicted by applying the STFT and the DGR. In the STFT, the Gaussian window was employed to exhibit a good time-frequency concentration, and a sufficient window length was given to offer the full Doppler resolution. However, the STFT is still limited in focusing the smeared image since several blurred parts still exist. On the other hand, the result of the DGR in Figure 7(b) shows significantly improved performance of ISAR image focusing in that prominent point-scatterers can be observed more clearly. We point out that the cross range resolution can be calculated from Figure 7 as follows:

$$\Delta r_{cr} = \frac{\lambda}{2\Delta\theta} = \frac{\lambda}{2 \times \Omega \times N \times M_p \times PRF^{-1}} \approx 0.071 \text{ m} \quad (7)$$

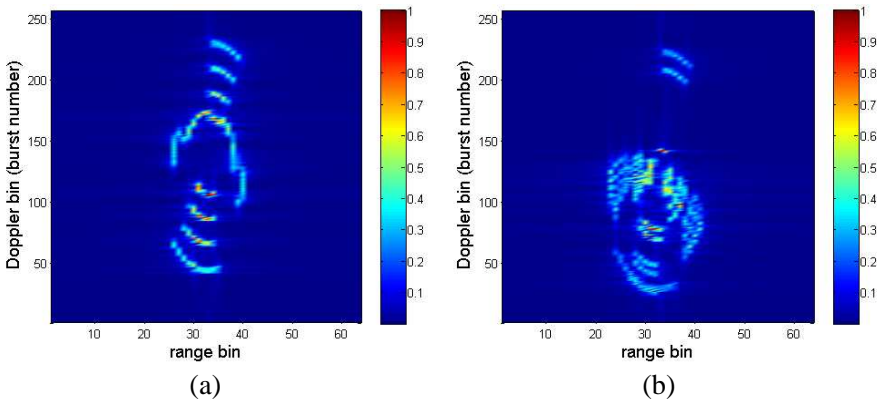


Figure 6. Conventional FT-based ISAR imaging of ideal point-scatterers: (a) set 1 and (b) set 2.

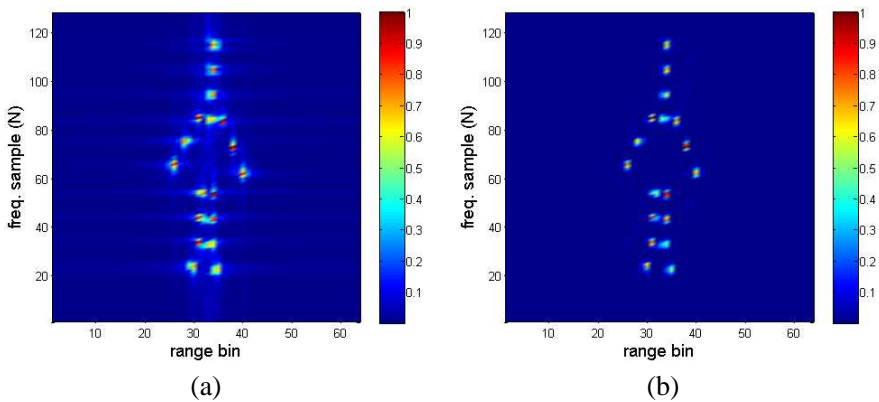


Figure 7. ISAR images of the ideal point-scatterer set 1 using: (a) STFT and (b) DGR with $Q = 32$.

The fact that the DGR is superior to the STFT is confirmed from Figure 8, which shows the time-frequency plots and the Doppler profiles of the time-domain signal at the selected 35th range cell. As observed in Figure 8(a), the DGR outperforms the STFT since the DGR concentrates the signal components on the time-frequency grid more effectively. The Doppler profiles in Figure 8(b) show that the DGR explicitly discriminates the Doppler frequency component induced by each prominent point-scatterer because of the compartmental assignment of $a_{m,n}$ and $h_{m,n}[k]$. With respect to computational efficiency, the calculation time of the DGR with $Q = 32$ is 0.697 sec,

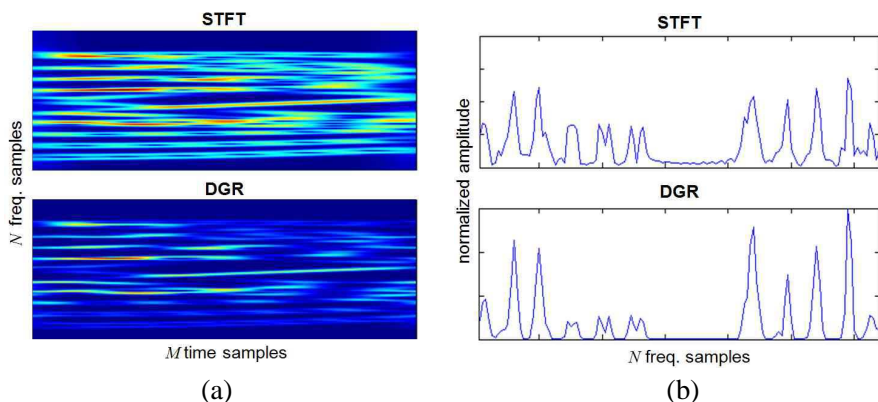


Figure 8. Comparison between the STFT and the DGR using the time-domain signal at the selected 35th range cell: (a) time-frequency plots and (b) Doppler profiles.

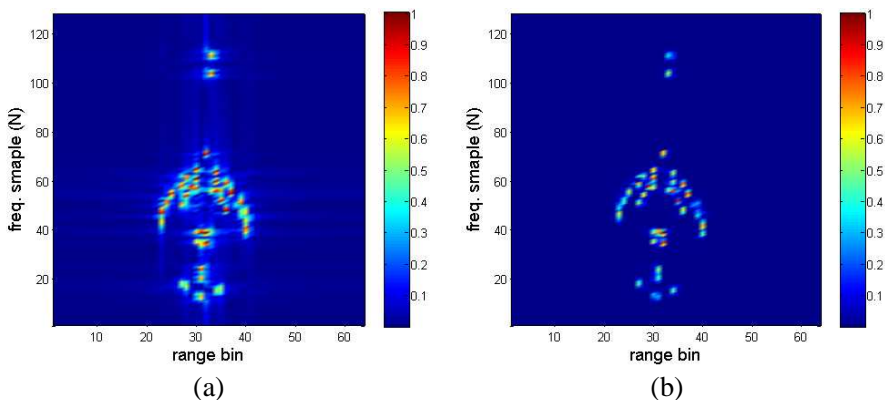


Figure 9. ISAR images of the ideal point-scatterer set 2 using: (a) STFT and (b) DGR with $Q = 32$.

which is only 1.13 times longer than that of the conventional FT. Figure 9 illustrates the ISAR images of the point-scatterer set 2 resulting from the STFT and the DGR, respectively.

4.2. Application to the Simulated MIG-25 Data

In the next example, we use the simulated radar signal data from the MIG-25 aircraft target composed of 120 point-scatterers. The radar center frequency is 9.0 GHz with a bandwidth of 512 MHz and

the PRF is 20 kHz. The numbers of pulses and bursts are given as 64 and 512, respectively. The angular speed of the target is $10^\circ/\text{s}$ on the assumption that the translational motion was perfectly compensated for. Figure 10 shows the ISAR images of the MIG-25 from various ISAR imaging methods. The ISAR image with the Gabor wavelet transform (GWT) [18] is also shown to compare the focusing performance. In this simulation, the DGR with $Q = 64$ was employed and each time-domain signal with a length of 512 was rearranged into the (256×128) time-frequency grid. The FT-based ISAR image in Figure 10(a) shows substantial image smearing by the time-varying Doppler frequency. Although both the STFT and the GWT obtain clear ISAR images, they are still restricted in removing image blurring. The ISAR image from the DGR, however, obviously reveals the enhanced focusing performance. The computation time of the DGR was 1.80 sec, 2.1 times slower than that of the FT.

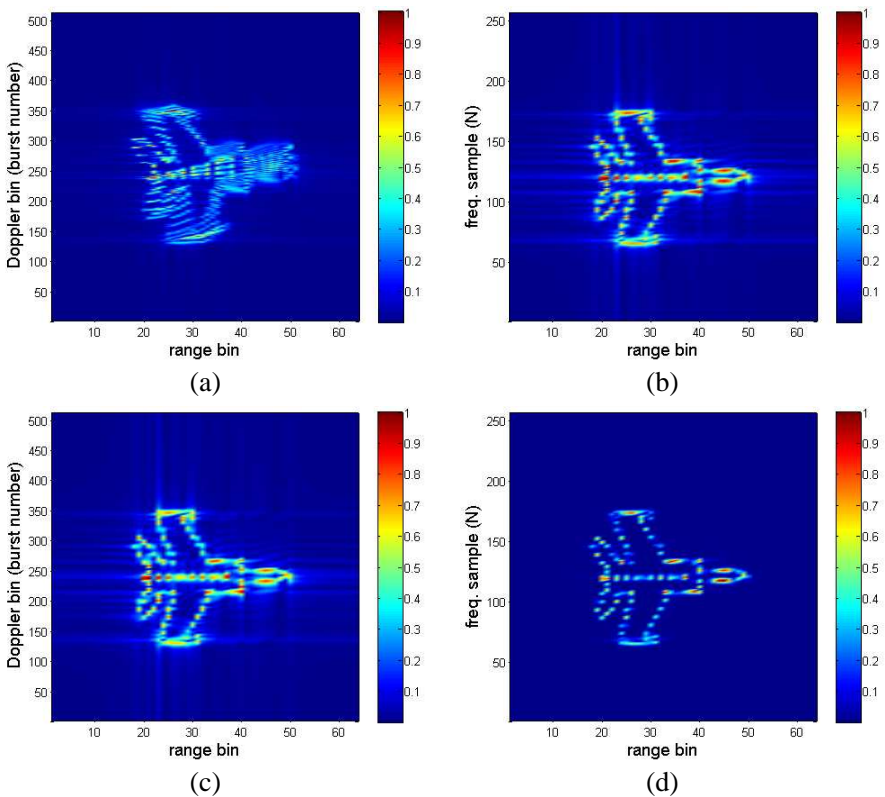


Figure 10. Simulation results of the MIG-25 using: (a) FT, (b) STFT, (c) GWT and (d) DGR with $Q = 64$.

4.3. Application to the Measured B-727 Data

For verifying applicability of the proposed method, we then utilize the real measured B-727 aircraft data, which was originally provided in the website. The radar center frequency is 9.0 GHz with a bandwidth of 150 MHz. The radar data with the SF waveform consists of 128 pulses and 128 bursts, respectively. Note that the cross range resolution cannot be obtained since the PRF and the motion parameters of the target are unknown. Figure 11 shows the ISAR images of the B-727 resulting from the FT and the DGR with an oversampling ratio of 32. From these images, the scattering phenomena from the fuselage and the tail are observed more distinctly than from the wing and the nose. For clearly indicating the prominent scattering parts, the ISAR images from the measured data were depicted by the different format of the color map. Compared to the FT-based image in Figure 11(a), the prominent parts of the target are well-focused in the DGR-based image in Figure 11(b). In addition, as explained earlier, the frequency components induced by noise appear to be suppressed by the excellent time-frequency concentration of the DGR. The computation time of the DGR is 0.795 sec, which is only 1.05 times slower than that of the FT. Thus, we demonstrated both focusing performance and efficiency of the DGR via the measured data.

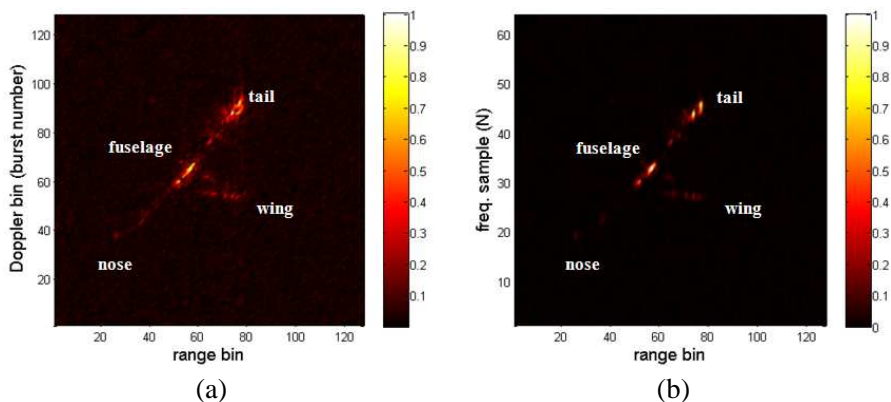


Figure 11. Application results of the measured B-727 data using: (a) FT and (b) DGR with $Q = 32$.

4.4. Discussion on Selection of the Oversampling Ratio Q

Here, we address the compromise between accuracy and efficiency related to selecting Q . Figure 12 illustrates the ISAR images of the MIG-25 for various values of Q at a different temporal frame (rotated

from the initial position). For the fixed number of frequency samples ($N = 256$), Figures 12(a) and 12(b) show high-quality ISAR images of the MIG-25 target and there is rarely a difference between these two images. As mentioned above, the larger Q needs more computation time. Thus, we select the oversampling ratio Q as 64 rather than 128 for which the computation time was 4.60 sec. Figure 12(c) shows the ISAR image from the DGR with $Q = 32$. The computation time was highly reduced to 0.93 sec at the expense of a slight degradation of image quality. However, the general shape of the MIG-25 is sufficiently discernible. For the case of $Q = 16$ shown in Figure 12(d), the computation time was only 0.49 sec. Nonetheless, the ISAR image is severely smeared as if two images of different temporal frames overlap each other. This phenomenon is caused by the lack of time samples related to the number of temporal frames.

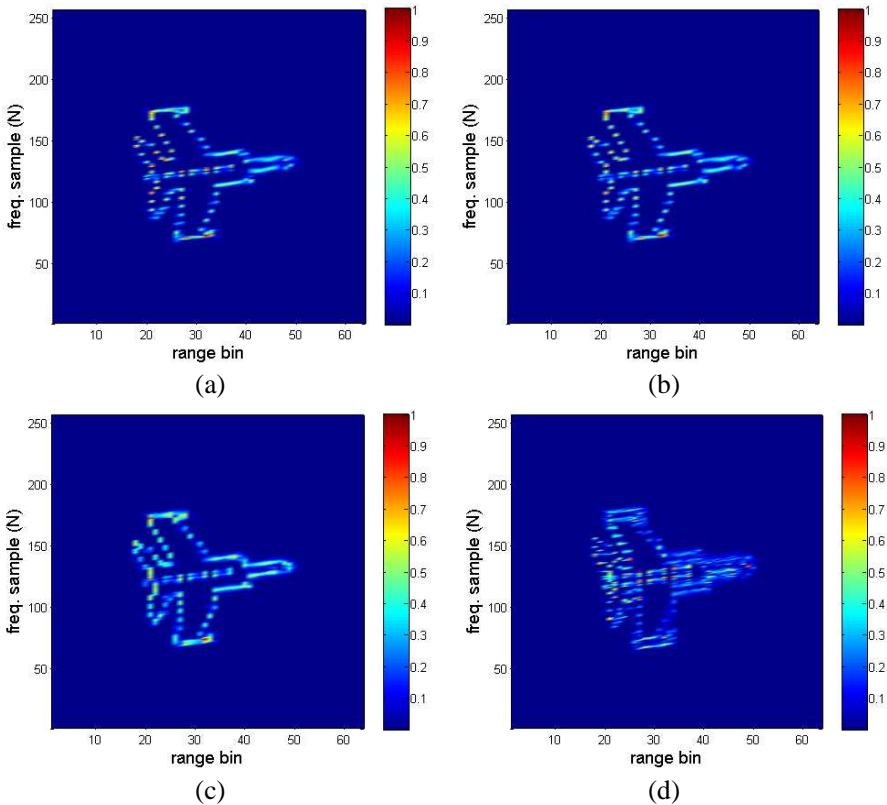


Figure 12. Simulation results of the MIG-25 at a different temporal frame using the DGR when Q is given as: (a) 128, (b) 64, (c) 32 and (d) 16.

From the comparison study with different values of Q , we find that in the MIG-25 simulation, $Q = 64$ is the optimal value in terms of compromise between image quality and a reasonable computation time. Q of 32 can also be a good candidate for fast computation. In the first example and third example, however, the optimal oversampling ratio was 32. It is seen that the optimal Q is dependent on the original number of bursts. Although a method for deterministically selecting Q should be developed in future studies, the DGR in the oversampling scheme demonstrated that it had outstanding performance in focusing ISAR images of moving targets. Furthermore, the DGR was proven to be suitable for being applied in real-time signal processing by selecting appropriate Q . This DGR-based ISAR image focusing can be further extended to a more efficient form by adopting recently proposed implementation algorithms as developed in [29, 30].

5. CONCLUSION

In this paper, we presented enhanced and efficient ISAR image focusing using the DGR in an oversampling scheme. With the oversampling scheme and analytically derived analysis window frames, the DGR yielded accurate Gabor coefficients denoting the amplitude of unit cells in the time-frequency grid. The compartmental allocation of Gabor coefficients and Gabor logons resulted in enhanced time-frequency concentration. Thus, the DGR is well-suited for applications of ISAR image focusing as evidenced by prominent point-scatterers being clearly discriminated. To validate the proposed approach, simulations of ISAR image focusing were carried out using the radar signal data from ideal point-scatterers and the MIG-25 aircraft. Application of the DGR to the measured data of the B-727 aircraft was also presented for verifying its applicability. The application results showed that the well-focused ISAR images were obtained within a computation time of less than 2 sec with the appropriate oversampling ratio Q . Therefore, we conclude that the DGR in the oversampling scheme can facilitate high-quality ISAR imaging by its enhanced focusing performance and computational efficiency.

ACKNOWLEDGMENT

This research was supported by Samsung Thales Co., Ltd.

REFERENCES

1. Chang, Y. L., C. Y. Chiang, and K. S. Chen, "SAR image simulation with application to target recognition," *Progress In Electromagnetics Research*, Vol. 119, 35–57, 2011.
2. Zhang, M., Y. W. Zhao, H. Chen, and W. Q. Jiang, "SAR imaging simulation for composite model of ship on dynamic ocean scene," *Progress In Electromagnetics Research*, Vol. 113, 395–412, 2011.
3. Wu, J., Z. Li, Y. Huang, Q. H. Liu, and J. Yang, "Processing one-stationary bistatic SAR data using inverse scaled Fourier transform," *Progress In Electromagnetics Research*, Vol. 129, 143–159, 2012.
4. Park, J. I. and K. T. Kim, "A comparative study on ISAR imaging algorithms for radar target identification," *Progress In Electromagnetics Research*, Vol. 108, 155–175, 2010.
5. Park, S. H., J. H. Lee, and K. T. Kim, "Performance analysis of the scenario-based construction method for real target ISAR recognition," *Progress In Electromagnetics Research*, Vol. 128, 503–518, 2012.
6. Calvo-Gallego, J. and F. Pérez-Martínez, "Simple traffic surveillance system based on range-Doppler radar images," *Progress In Electromagnetics Research*, Vol. 125, 343–364, 2012.
7. Buddendick, H. and T. F. Eibert, "Bistatic image formation from shooting and bouncing rays simulated current distributions," *Progress In Electromagnetics Research*, Vol. 119, 1–18, 2011.
8. Jia, Y., L. Kong, and X. Yang, "A novel approach to target localization through unknown walls for through-the-wall radar imaging," *Progress In Electromagnetics Research*, Vol. 119, 107–132, 2011.
9. Felguera-Martin, D., J. T. Gonzalez-Partida, and M. Burgos-Garcia, "Interferometric ISAR imaging on maritime target applications: Simulation of realistic targets and dynamics," *Progress In Electromagnetics Research*, Vol. 132, 571–586, 2012.
10. Park, S. H., J. I. Park, and K. T. Kim, "Motion compensation for squint mode spotlight SAR imaging using efficient 2D interpolation," *Progress In Electromagnetics Research*, Vol. 128, 503–518, 2012.
11. Liu, B. and W. Chang, "Range alignment and motion compensation for missile-borne frequency stepped chirp radar," *Progress In Electromagnetics Research*, Vol. 136, 523–542, 2013.
12. Jeong, H. R., H. T. Kim, and K. T. Kim, "Application of subarray averaging and entropy minimization algorithm to

- stepped-frequency ISAR autofocus,” *IEEE Trans. Antennas and Propagation*, Vol. 56, No. 4, 1144–1154, 2008.
13. Kirkland, D. M., “An alternative range migration correction algorithm for focusing moving targets,” *Progress In Electromagnetics Research*, Vol. 131, 227–241, 2012.
 14. Liu, B. and W. Chang, “A novel range-spread target detection approach for frequency stepped chirp radar,” *Progress In Electromagnetics Research*, Vol. 131, 275–292, 2012.
 15. Chen, V. C. and H. Ling, *Time-frequency Transforms for Radar Imaging and Signal Analysis*, Artech House, Norwood, MA, 2002.
 16. Chen, V. C. and S. Qian, “Joint time-frequency transform for radar range-Doppler imaging,” *IEEE Trans. Aerospace and Electronic Systems*, Vol. 34, No. 2, 486–499, 1998.
 17. Hajduch, G., J. M. LevCallec, and R. Garello, “Airborne high-resolution ISAR imaging of ship targets at sea,” *IEEE Trans. Aerospace and Electronic Systems*, Vol. 40, No. 1, 378–384, 2004.
 18. Shin, S. Y. and N. H. Myung, “The application of motion compensation of ISAR image for a moving target in radar target recognition,” *Microwave and Optical Technology Letters*, Vol. 50, No. 6, 1673–1678, 2008.
 19. Berizzi, F., E. D. Mese, M. Diani, and M. Martorella, “High-resolution ISAR imaging of maneuvering targets by means of the range instantaneous Doppler technique: Modeling of the range instantaneous Doppler,” *IEEE Trans. Image Processing*, Vol. 10, No. 12, 1880–1890, 2001.
 20. Peng, J., L. Dan, D.Liu, G.-M. Wang, and H. Yuan, “Reconstruction of ISAR imaging using time-frequency distribution series method,” *1st Asian and Pacific Conference on Synthetic Aperture Radar*, 351–354, China, Nov. 2007.
 21. Choi, I. S., B. L. Cho, and H. T. Kim, “ISAR motion compensation using evolutionary adaptive wavelet transform,” *IEE Proc. Radar, Sonar and Navigation*, Vol. 150, No. 4, 229–233, 2003.
 22. Thayaparan, T., G. Lampropoulos, S. K. Wong, and E. Riseborough, “Application of adaptive joint time-frequency algorithm for focusing distorted ISAR images from simulated and measured radar data,” *IEE Proc. Radar, Sonar and Navigation*, Vol. 150, No. 4, 213–220, 2003.
 23. Brinkman, W. and T. Thayaparan, “Focusing ISAR images using the AJTF optimized with the GA and the PSO algorithm-comparison and results,” *2006 IEEE Conference on Radar*,

- Canada, Apr. 2006.
24. Du, L and G. Su, "Adaptive inverse synthetic aperture radar imaging for nonuniformly moving targets," *IEEE Geoscience and Remote Sensing Letters*, Vol. 2, No. 3, 247–249, 2005.
 25. Thayaparan, T., L. J. Stankovic, C. Wernik, and M. Dakovic, "Real-time motion compensation, image formation and image enhancement of moving targets in ISAR and SAR using S-method-based approach," *IET Signal Processing*, Vol. 2, No. 3, 247–264, 2008.
 26. Wexler, J. and S. Raz, "Discrete Gabor expansion," *Signal Processing*, Vol. 21, No. 3, 207–220, 1990.
 27. Zibulski, M. and Y. Y. Zeevi, "Oversampling in Gabor scheme," *IEEE Trans. Signal Processing*, Vol. 41, No. 8, 2679–2985, 1993.
 28. Bastiaans, M. J., "Gabor's signal expansion and the Zak transform," *Applied Optics*, Vol. 33, No. 23, 5241–5255, 1994.
 29. Strohmer, T., "Approximation of dual Gabor frames, window decay, and wireless communications," *Applied and Computational Harmonic Analysis*, Vol. 11, 243–262, 2001.
 30. Sondergaard, P. L., "Efficient algorithms for the discrete Gabor transform with a long FIR window," *Journal of Fourier Analysis and Applications*, Vol. 18, No. 3, 456–470, 2012.
 31. Zhang, X., J. Qin, and G. Li, "SAR target classification using Bayesian compressive sensing with scattering centers features," *Progress In Electromagnetics Research*, Vol. 136, 385–407, 2013.